



Fabrication of carbon bridged $g\text{-C}_3\text{N}_4$ through supramolecular self-assembly for enhanced photocatalytic hydrogen evolution



Huiliang Li^a, Fengping Li^b, Zeyan Wang^{a,*}, Yachen Jiao^a, Yuanyuan Liu^a, Peng Wang^a, Xiaoyang Zhang^a, Xiaoyan Qin^a, Ying Dai^b, Baibiao Huang^{a,*}

^a State Key Laboratory of Crystal Materials, Shandong University, Jinan 250100, China

^b School of Physics, Shandong University, Jinan 250100, China

ARTICLE INFO

Keywords:

Supramolecular self-assembly
Carbon-bridged $g\text{-C}_3\text{N}_4$
Delocalized big π bonds
Photocatalysis
Hydrogen generation

ABSTRACT

Carbon bridged graphitic carbon nitride ($g\text{-C}_3\text{N}_4$) was prepared by a facile supramolecular self-assembly method. Experimental results and theoretical calculations indicate C atoms were introduced into the $g\text{-C}_3\text{N}_4$ lattice by substituting the bridged N atoms. As a result, the delocalized big π bonds can be formed among the adjacent heptazine rings, which could both enhance the light absorption and promote the charge separation. Beneficial from the efficient charge separation and enhanced light absorption, the carbon bridged $g\text{-C}_3\text{N}_4$ exhibits high efficient photocatalytic activity, where the H_2 evolution rate is about 7 times as high as that of pristine $g\text{-C}_3\text{N}_4$. This work demonstrates carbon bridged C_3N_4 can be fabricated by a simple supramolecular self-assembly process, which could be useful for the further development of high efficient $g\text{-C}_3\text{N}_4$ photocatalysts.

1. Introduction

The challenges of rapid consumption of fossil fuels and increase of critical environment destruction have invigorated growing awareness in the past few decades [1,2]. Photocatalysis, as one of most potential technologies on utilizing solar energy, has gained considerable attention for its diverse potential on energy and environmental applications [3,4]. Up to now, large quantities of semiconductor-based photocatalysts have been investigated, such as TiO_2 [5,6], ZnO [1], BiOX [7], etc. However, these photocatalysts usually suffer from the poor light absorption or low stability. Thus, the exploration of new photocatalysts with wider light absorption spectra and higher stability has become a hot spot in photocatalysis.

As a promising metal-free photocatalyst, $g\text{-C}_3\text{N}_4$ has attracted increasing attention in recent years due to its facile synthesis, appealing electronic band structures, high physicochemical stability, and “earth-abundant” reserves [8,9]. Moreover, $g\text{-C}_3\text{N}_4$ has been demonstrated as a very promising solar-energy-driven photocatalyst for hydrogen evolution because of its appropriate band position. However, with a band gap of 2.7 eV, pure $g\text{-C}_3\text{N}_4$ can only absorb visible light up to 450 nm, which can only utilizing parts of the visible solar spectrum. Additionally, the carrier mobility in $g\text{-C}_3\text{N}_4$ is quite low, which result in high charge recombination rate in $g\text{-C}_3\text{N}_4$ that further restrict the photocatalytic H_2 evolution activity. Thus, more efforts are still needed to address the above problems and further improve the photocatalytic activity of $g\text{-C}_3\text{N}_4$.

C_3N_4 . Up to now, various strategies have been developed to further improve the photocatalytic activity of $g\text{-C}_3\text{N}_4$ such as anion doping [10–13], constructing heterojunctions [13–17], nanostructure modulations, etc. [18–20]. Among these, doping is considered as one of the most effective and simplest methods to improve the photocatalytic activity of $g\text{-C}_3\text{N}_4$. For example, doping $g\text{-C}_3\text{N}_4$ with non-metallic elements, such as P, S, or I, could greatly improve the hydrogen evolution rate by narrowing the band gap and increase the electric conductivity of $g\text{-C}_3\text{N}_4$ [21]. However, on the other hand, doping could introduce foreign impurities to the materials, which would act as defects and recombination centers for photogenerated charge carriers, thus, lower the photocatalytic activity. Recently, self-doped $g\text{-C}_3\text{N}_4$ have been reported by substituting some N atoms with C atoms, which has been demonstrated to be a more effective method to further improve the photocatalytic activity of $g\text{-C}_3\text{N}_4$ [22–25]. Self-doping can not only expand the visible light absorption of $g\text{-C}_3\text{N}_4$, but also be able to facilitate the charge transfer among heptazine units by forming big π bonds among the heptazine units if the bridged N atoms could be substituted by C atoms. Thus, the photogenerated carriers can be transferred much easier among the heptazine units, thereby improving the photocatalytic activity. However, the fabrication of carbon self-doped $g\text{-C}_3\text{N}_4$ is still challenging owing to the absence of any oxygen and metal elements in $g\text{-C}_3\text{N}_4$.

Supramolecular self-assembly is the process that molecules adopt a well-defined arrangement into stable aggregates by non-covalent bonds

* Corresponding authors.

E-mail addresses: wangzeyan@sdu.edu.cn (Y. Jiao), bbhuang@sdu.edu.cn (B. Huang).

under equilibrium conditions, which has been widely used in crystal engineering, molecular recognition and catalysis, etc. [26]. Due to the supramolecular aggregates with tunable morphologies between melamine and triazine derivatives, e.g., cyanuric acid, supramolecular self-assembly has recently been widely used to synthesize $g\text{-C}_3\text{N}_4$ with various morphologies to further improve their photocatalytic activities [27,28]. However, it has not been used to fabricate carbon self-doped $g\text{-C}_3\text{N}_4$ by supramolecular self-assembly till to now. Chitosan, as the second most abundant polysaccharide in nature, has been widely used in biomedical applications due to its excellent biocompatibility and biodegradability. Since chitosan backbone contains many functional groups, like $-\text{OH}$, $-\text{NH}_2$ and $-\text{NHCOCH}_3$, self-assembly aggregates can be easily formed between chitosan and other molecules by various non-covalent interactions, such as hydrogen bonds, electrostatic interactions, hydrophobic interactions, and van der Waals forces [29,30]. Thus, it would be possible for melamine to link with chitosan to form self-assembly aggregates, which could act as the precursor to prepare carbon self-doped $g\text{-C}_3\text{N}_4$ owing to the high carbon contents in chitosan.

In this work, we prepared carbon self-doped $g\text{-C}_3\text{N}_4$ by supramolecular self-assembly method. Experimental and theoretical results indicate C atoms have been introduced to the lattice of $g\text{-C}_3\text{N}_4$ by substituting the bridged N atoms in the as-prepared CCN-x samples. As a result, the light absorption and the charge separation of CCN-x samples were greatly improved owing to the formation of delocalized big π bonds. And CCN-1 exhibits the highest photocatalytic activity during the photocatalytic H_2 evolution experiments, which is about 7 times that of the pristine $g\text{-C}_3\text{N}_4$. This indicates supramolecular self-assembly could be used as a potential method to fabricate highly efficient carbon bridged $g\text{-C}_3\text{N}_4$ photocatalysts with delocalized big π bonds.

2. Experimental section

2.1. Fabrication of carbon self-doped $g\text{-C}_3\text{N}_4$

In a typical synthesis, 1 g melamine powders (Tianjin Kemiou Chemical Regent Co. Ltd.) was initially dissolved in 300 mL deionized water. Then, certain amount of chitosan (Aladdin reagent) (e.g., 0.005, 0.01, 0.025, 0.05, 0.1 g) were added into the melamine solution with continuous stirring. The mixed solution was stirred for 4 h at room temperature, then dried at 80 °C. Finally, the mixture were ground into powder and calcined at 550 °C for 4 h with a heating rate of 5.0 °C min⁻¹ in air atmosphere. After cooling to room temperature, the resultant $g\text{-C}_3\text{N}_4$ samples were collected and ground into powders before use. The samples were denoted as CCN-x (x = 0.5, 1, 2.5, 5 or 10, corresponding to the mass percentage of chitosan to melamine, respectively.). For comparison, pure $g\text{-C}_3\text{N}_4$ was also synthesized following the same procedure in the absence of chitosan, which was denoted as $g\text{-C}_3\text{N}_4$.

2.2. Characterizations

X-Ray diffraction (XRD) characterizations were performed on a Bruker D8 advanced X-ray powder diffractometer with Cu K α radiation ($\lambda = 1.5418 \text{ \AA}$). Scanning electron microscopy (SEM) images were obtained with a Hitachi S-4800 microscope. Transmission electron microscopy (TEM), high-resolution transmission electron microscopy (HRTEM) measurements were carried out on a JEOL-F2100 microscope. The UV-vis diffuse reflectance spectra (UV-vis DRS) were measured on a Shimadzu UV 2550 UV/vis spectrophotometer, which was equipped with an integrating sphere, and BaSO₄ was used as a reference. The BET surface area was determined using N₂ adsorption/desorption isotherm measurements by a Micromeritics ASAP 2020 apparatus. X-ray Photoelectron Spectroscopy (XPS) spectra were measured in a Thermo Fisher Scientific Escalab 250 spectrometer with monochromatized Al K α excitation, and C_{1s} (284.6 eV) was used to calibrate the peak

positions of the elements. The PL spectra were measured on a Hitachi F-4500 fluorescence spectrophotometer at room temperature and obtained with excitation wavelength at 350 nm.

2.3. Photocatalytic experiments

The photocatalytic activities of the as-synthesized samples were evaluated by photocatalytic hydrogen evolution in a Pyrex top-irradiation reaction vessel connected to a closed glass gas system. Typically, 100 mg of catalyst powder was dispersed in 100 mL aqueous solution containing 10 vol % triethanolamine as sacrificial electron donor and 3 wt % H₂PtCl₆·6H₂O as co-catalyst during the reaction. The reaction solution was evacuated several times to remove air completely prior to irradiation under a 300 W Xeon-lamp equipped with a 420 nm-cut-off filter. The temperature of the reaction solution was maintained at 10 °C during the entire reaction. The evolved gas was analyzed by gas chromatography equipped with a thermal conductivity (TCD) detector using high-purity argon carrier gas.

2.4. Photoelectrochemical tests

Photoelectrochemical tests were conducted in a three-electrode system with a potentiostat (Princeton Applied Research, Model 263A), where the C_3N_4 electrode, a saturated Ag/AgCl and a platinum plate act as the working electrode, reference electrode and counter electrode, respectively. An aqueous solution of 0.5 M Na₂SO₄ was used as the electrolyte. The C_3N_4 working electrode was prepared by spin-coating photocatalyst slurry on an F-doped tin oxide (FTO) glass electrode and subsequently heating at 100 °C for 0.5 h. The working electrode was illuminated with AM 1.5G simulated sunlight (100 mW cm⁻²). The photocurrent was measured at 1.23 V vs RHE. Potentiostatic electrochemical impedance spectroscopy (EIS) was carried out at a dc potential 1.23 V vs RHE with an ac potential frequency range from 100,000 to 0.1 Hz.

2.5. Theoretical calculations

The first-principles DFT electronic calculations are adopted using the projector augmented wave (PAW) method as implemented in the plane-wave basis code Vienna ab initio Simulation Package (VASP) [31]. The generalized gradient approximation (GGA) for exchange-correlation functional is performed in the framework of Perdew, Burke, and Ernzerhof (PBE) parametrization [32]. The Monkhorst-Pack (MP) grid of $7 \times 7 \times 1$ is adopted for Brillouin zone integrations during geometry relaxation and electronic structure calculations of pure $g\text{-C}_3\text{N}_4$ and other three substitutive $g\text{-C}_3\text{N}_4$ [33]. The cutoff energy for the plane wave basis is set as 400 eV, and the vacuum spacing larger than 15 Å is added along the z direction to avoid the spurious interactions between neighboring images. Additionally, the atomic forces are relaxed until they are converged within 0.01 eV Å⁻¹ in the process of the atomic structure optimization by means of a conjugate gradient method. The ionic relaxation convergence criterions is chosen as 10⁻⁵ eV.

3. Results and discussion

The supramolecular aggregates formed between chitosan and melamine are denoted as MC-x, where x is the mass ratio of melamine to chitosan. As a represent, MC-5 were characterized by XRD as shown in Fig. 1a. In addition of the XRD peaks of melamine and chitosan, several new peaks can be observed in MC-5 aggregates, indicating the formation of crystalline melamine-chitosan complex through self-assembly. MC-5 samples were further characterized by FT-IR spectra. As shown in Fig. 1b, no new peaks appear in the MC-5 compared with melamine, but the C=N stretching vibration of MC-5 shifted to higher wavenumbers in comparison with melamine from 1532.5 to 1548.3 cm⁻¹ (Fig. 1b,

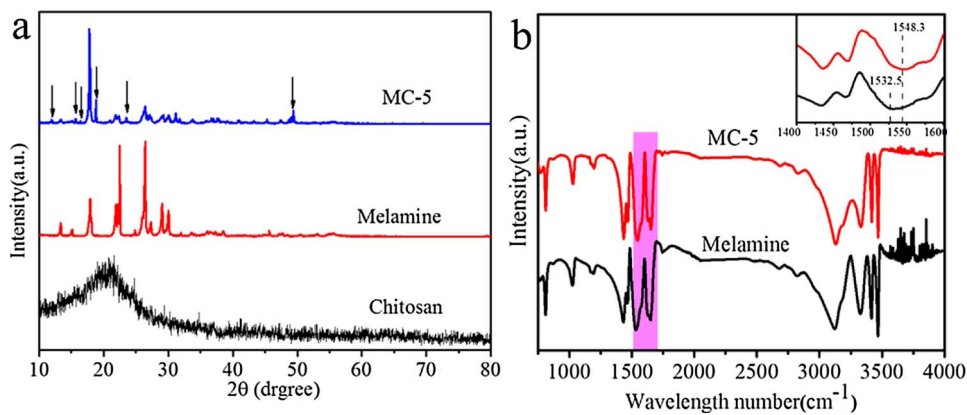


Fig. 1. (a) XRD patterns and (b) FT-IR spectra of melamine and MC-5.

inset), suggesting the rearranged structure in the aggregate, which can be further indicated by the small blue shift of the peaks of N–H stretching vibrations between 3000 and 3500 cm^{-1} , deformation vibrations of N–H at 1652 cm^{-1} and C–N stretching vibration at 1026 cm^{-1} [26,34].

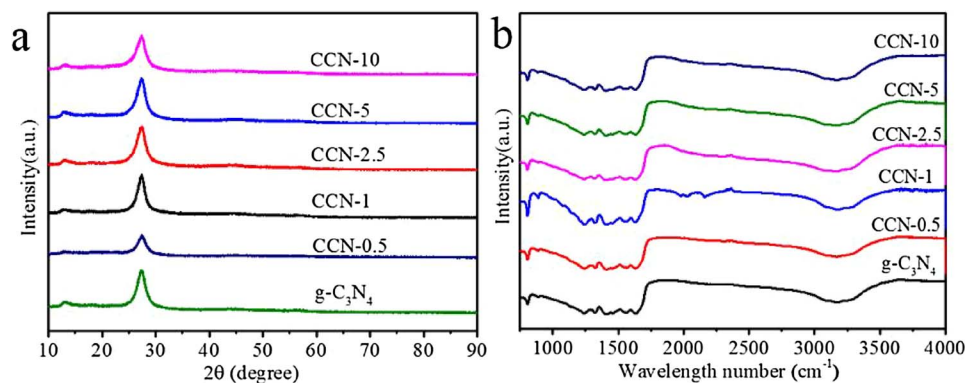
After calcination at 550 $^{\circ}\text{C}$ for 4 h, the supramolecular aggregates were transformed to g-C₃N₄, which were denoted as CCN-x (x refers to the mass percentage of chitosan to melamine). All the CCN-x samples exhibit two distinct diffraction peaks at 13.0° and 27.4°, corresponding to the (100) in-plane repeating motifs of continuous heptazine framework and the (002) reflection of graphitic structure of g-C₃N₄, respectively (Fig. 2a). This indicates the CCN-x samples prepared through self-assembly retained the conjugated structure of g-C₃N₄. To be noticed, the peak at 13.0° became weaker in comparison with pristine g-C₃N₄, which could be attributed to the carbon doping into g-C₃N₄ crystal lattice [27]. To further investigate the molecular structure of as-prepared CCN-x, FT-IR measurements were performed. As shown in Fig. 2b, for all the CCN-x samples, the FT-IR spectra are almost identical with that of pristine g-C₃N₄, where all the characteristic peaks of g-C₃N₄ at 810, 1200–1600 and 3000–3700 cm^{-1} , corresponding to the s-triazine ring, C–N heterocycles and stretching vibration for –NH, respectively, can be clearly observed. These results further confirm the as-prepared CCN-x samples are graphic carbon nitrides, which can be prepared from supramolecular aggregates.

As a method to tune the morphology of g-C₃N₄, the samples prepared by self-assembly are usually different from that prepared from melamine precursors [27,35]. However, as shown in the SEM images in Fig. S1a and b, the morphologies of CCN-x samples prepared in this work are quite similar as that of pristine g-C₃N₄, which are primarily irregular aggregates consisted of stacked nanosheets. For a closer observation, as shown in the TEM images in Fig. S1c and d, the pristine g-C₃N₄ is mainly consisted of some smooth nanosheets with sizes of

~400 nm, while CCN-x samples (e.g., CCN-1) are consisted of some wrinkled nanosheets of ~800 nm, which indicate the thinner thickness of the nanosheets in CCN-x samples as observed in other 2D materials [36]. However, the differences on morphologies have little effects on the surface areas and pore size distribution of as-prepared CCN-x samples as shown in Fig. S2. For example, the surface area of CCN-0.5 is 17.4 $\text{m}^2 \text{g}^{-1}$, which is almost the same as that of pristine g-C₃N₄ (17.8 $\text{m}^2 \text{g}^{-1}$).

Although the XRD patterns, FT-IR spectra and the morphologies of as-prepared CCN-x samples are almost the same as that of pristine g-C₃N₄ (Fig. 2a and b), their colors are quite different as shown in the photographs in Fig. 3a. With the increase of x, the color of CCN-x gradually becomes deeper, turning from light yellow to dark brown. UV-vis diffused reflectance spectra (DRS) as shown in Fig. 3b further confirm the color variation. In comparison to pristine g-C₃N₄, a continuous increase on light absorption background can be clearly observed in CCN-x samples in the longer wavelength range ($\lambda > 450 \text{ nm}$) with the increase of x values. Elemental analyses were carried out to investigate the change on C/N ratios in CCN-x samples. As shown in Table S1, the C/N ratios of CCN-x samples are slightly higher than that of pristine g-C₃N₄, and gradually increased with the increase of x values. This indicates the color variation and the enhanced light absorption background could be mainly ascribed to the increased carbon contents in the as-prepared CCN-x samples. However, the extra carbon in CCN-x can be existed either in the form of amorphous C adsorbed on the surface of the samples, or lattice C by substituting the N atoms in C₃N₄ matrix, because both of them can enhance the light absorption background of g-C₃N₄.

In order to identify the states of C in CCN-x samples, thermogravimetric analyses (TGA) were carried out. As a representative, CCN-1 was chosen to compare with pristine g-C₃N₄ and chitosan. As shown in Fig. 4a, chitosan began to decompose at ~500 $^{\circ}\text{C}$ and was completely

Fig. 2. (a) XRD patterns and (b) FT-IR spectra of pristine g-C₃N₄ and CCN-x.

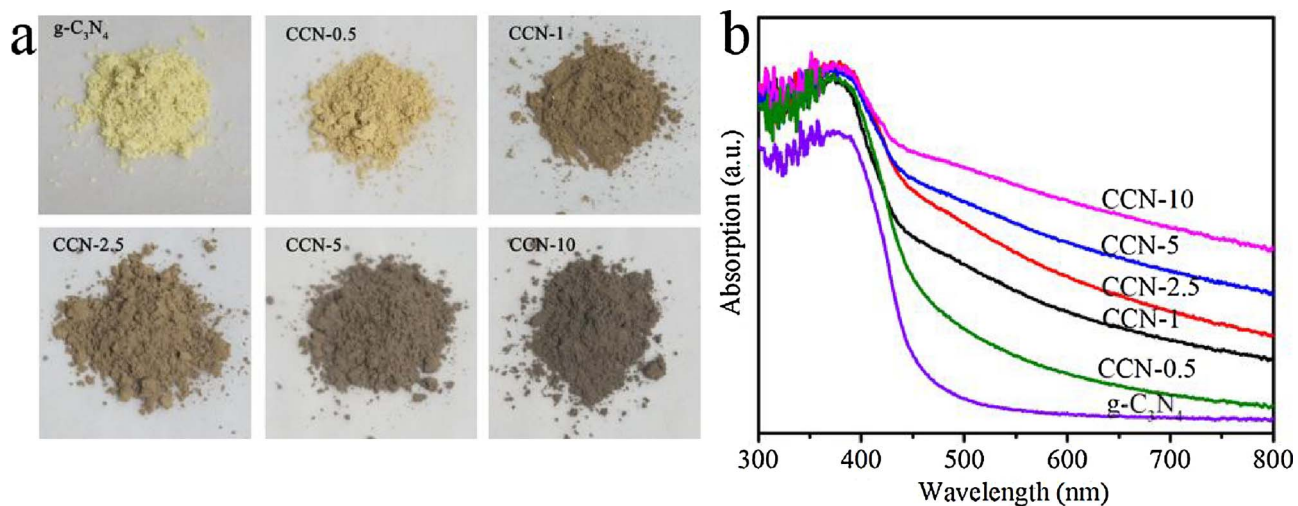


Fig. 3. (a) Photographs and (b) UV-vis DRS spectra of pristine $\text{g-C}_3\text{N}_4$ and CCN-x.

decomposed at 570°C . Thus, at the synthetic temperature of 550°C , most of chitosan in the self-assembly aggregates can be decomposed. And indeed, no obvious weight loss can be observed from the TGA curve of CCN-1 as the temperature is below 600°C , indicating no amorphous C existed in CCN-1. To further prove this, we prepared CCN-1 samples at 600°C (CCN-1-600). The DRS spectra of CCN-1-600 is almost the same as that of CCN-1 prepared at 550°C (Fig. 4b). This could exclude the existence of amorphous C in as-prepared CCN-1. To be noticed, the decomposition temperature of CCN-1 is much lower than that of pristine $\text{g-C}_3\text{N}_4$ (650 vs 700°C). This could be an indicative of C doping to substitute the N atoms in $\text{g-C}_3\text{N}_4$, because the bond energy of C–C bond is smaller than that of C–N bond [37]. To further prove the C doping in CCN-1, XPS measurements were performed. As shown in Fig. 4c, the N 1s XPS spectra of CCN-1 and pristine $\text{g-C}_3\text{N}_4$ can be deconvoluted into three bands of C–N=C peak at 398.6 , N–(C)₃ peak at 399.9 and N–H peak at 401.3 eV, respectively. And the peak area ratio corresponding to N–(C)₃ for pristine $\text{g-C}_3\text{N}_4$ and CCN-1 is calculated to be 0.117 and 0.113 , respectively. This demonstrates that the N atoms in $\text{g-C}_3\text{N}_4$ have partially substituted by C atoms in CCN-1 [20]. And the C doping concentration is calculated to be 3.4% for CCN-1.

There are three different N sites in $\text{g-C}_3\text{N}_4$ as labeled in Fig. 5. In order to probe which N site could be most likely substituted by C atoms, the total energies were calculated by substituting the N with C at the three different sites. As shown in Fig. 5a, the total energy by substituting the N atoms at site 1 to 3 is calculated to be -118.00 , -116.49 and -118.13 eV, respectively. That indicates the substitution at site 1 and 3 is more favorable, as the total energies are lower than that of the pristine $\text{g-C}_3\text{N}_4$ (-117.74 eV). From the aspect of total energy, site 1 is more preferred than site 3 for C doping due to its slightly

lower total energy. However, considering the larger stereo-hindrance effect in site 3, site 1 could be the most preferable site for C doping from the aspect of kinetics.

In order to further understand the effects of C doping on the charge transfer and separation in $\text{g-C}_3\text{N}_4$, DFT calculations were performed. Fig. 5b–d shows the density of states of pristine $\text{g-C}_3\text{N}_4$ and the C doped C_3N_4 at site 1 and site 3, respectively. It is well known that the charge transfer and separation is mainly determined by the π bonds characters, which were directly decided by the electron orbital of P_z . Fig. 5b–d shows the contribution of P_z electron orbitals in the total density of states (TDOS) in pristine $\text{g-C}_3\text{N}_4$, and C doped C_3N_4 at site 1 and 3, respectively. It is clearly to see that the C substitution in the site 1 possess more contributions near the Fermi level and has a sharper peak in comparison with the other conditions. This suggests the doping in site 1 is more favorable for the formation of delocalized big π bonds, which would extend the light absorption (as shown in Fig. 3) and favor the electrons transfer among the adjacent heptazine units. Therefore, the CCN-x samples prepared in this work are mainly C bridged $\text{g-C}_3\text{N}_4$ by substituting the bridged N atoms, which are expected to have higher photocatalytic activities than pristine $\text{g-C}_3\text{N}_4$ owing to the enhanced light absorption and improved charge separation.

In order to evaluate the photocatalytic properties of as-prepared CCN-x samples, photocatalytic H_2 evolution experiments were carried out under visible light irradiation ($\lambda > 420$ nm). As shown in Fig. 6a and b, as-expected all CCN-x samples exhibit higher photocatalytic H_2 evolution activity in comparison with pristine $\text{g-C}_3\text{N}_4$. Among those, CCN-1 shows the highest H_2 evolution rate of $52.9 \mu\text{mol h}^{-1}$, which is about 7 times that of pristine $\text{g-C}_3\text{N}_4$ ($7.9 \mu\text{mol h}^{-1}$). To exclude the effects of surface areas, the H_2 evolution rates were normalized to the surface areas of the samples. As shown in Fig. 6b, CCN-1 still exhibit the

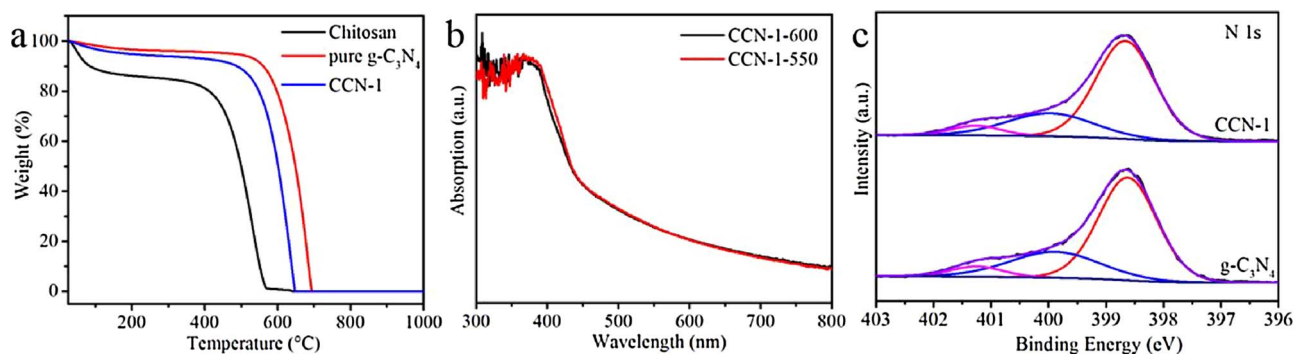


Fig. 4. (a) TGA curves of chitosan, pristine $\text{g-C}_3\text{N}_4$ and CCN-1. (b) UV-vis spectra of CCN-1-600 and CCN-1-550. (c) N 1s XPS spectra of pristine $\text{g-C}_3\text{N}_4$ and CCN-1.

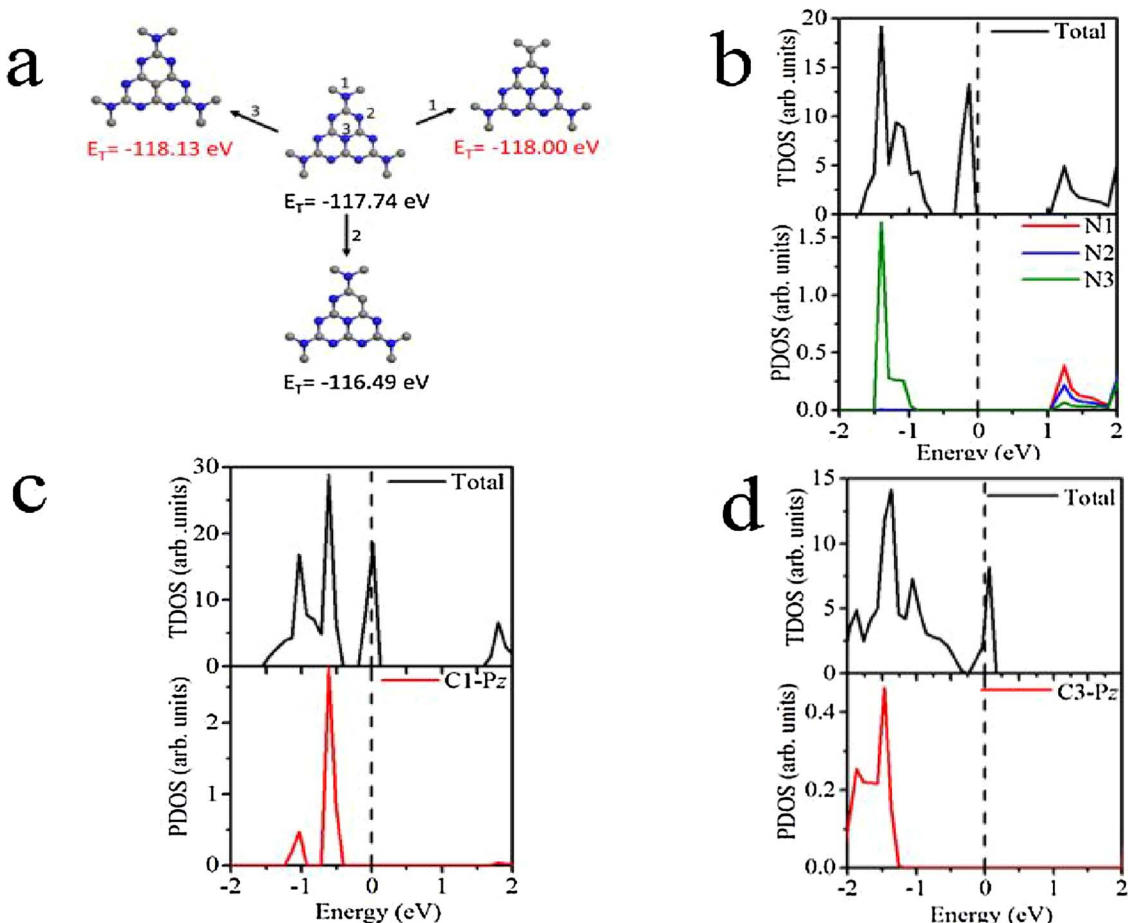


Fig. 5. (a) Calculated total energy (E_T) of pristine $\text{g-C}_3\text{N}_4$ and carbon bridged $\text{g-C}_3\text{N}_4$ through substituting N (site 1–3) by carbon atom (C, N are indicated by grey and blue spheres, respectively) and (b, c, d) calculated TDOS and the DOS of P_z electron orbital of pristine $\text{g-C}_3\text{N}_4$ and carbon doping by substitute site 1 and 3.

highest H_2 evolution rate ($\sim 22 \mu\text{mol h}^{-1} \text{m}^{-2}$), which is about 5 times as that of pristine $\text{g-C}_3\text{N}_4$. In order to test the stability of CCN-1, cycling experiments were carried out as shown in Fig. 6c. After photocatalytic H_2 evolution for 40 h, CCN-1 is still highly reactive, with only a slightly decrease on H_2 evolution rate, which could be ascribed to the dropping off of the cocatalyst that has been observed by other researchers [36]. These results suggest the carbon bridged $\text{g-C}_3\text{N}_4$ has good photocatalytic activity and cycling stability.

To further understand the mechanism for the enhanced photocatalytic activity, the charge separation and migration process in CCN-1 and pristine $\text{g-C}_3\text{N}_4$ were investigated. As shown in Fig. S3, CCN-1 shows three fold enhancement on photocurrent comparing to pristine $\text{g-C}_3\text{N}_4$, suggesting more efficient charge separation in CCN-1.

Electrochemical impedance spectra (EIS) analysis was further employed to analyze the charge separation properties. Fig. 7a shows the Nyquist plots of CCN-1 and pristine $\text{g-C}_3\text{N}_4$, respectively. As the semi-circle in Nyquist plot at high frequencies is the characteristic of the charge transfer process, the smaller diameter of the semicircle for CCN-1 in comparison with $\text{g-C}_3\text{N}_4$ indicates the smaller charge transfer resistance in CCN-1. As another method to probe the photogenerated charge separation and recombination, photoluminescence (PL) spectra were also performed. As shown in Fig. 7b, pristine $\text{g-C}_3\text{N}_4$ shows a strong PL peak at 470 nm, corresponding to the direct electron-hole recombination of band transition [38]. However, a sharp decrease on PL peak intensity can be observed in CCN-1, which indicates reduced charge recombination and accelerated charge migration among

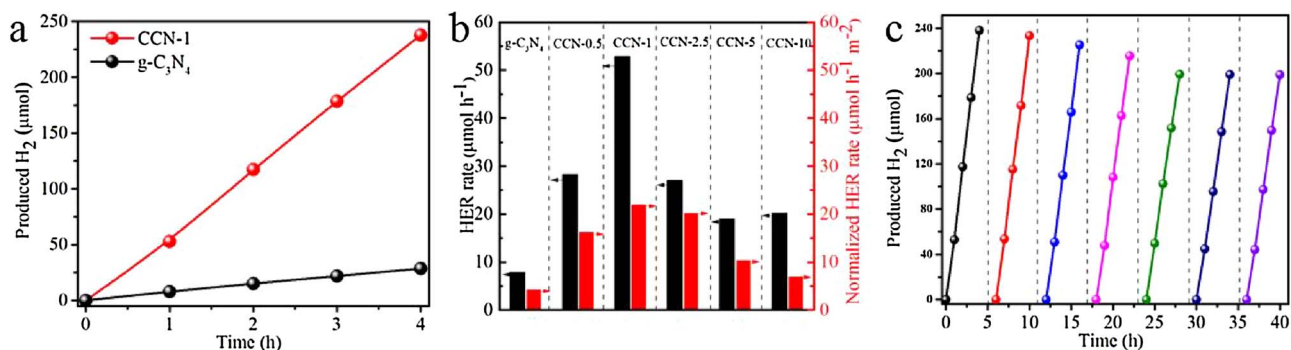
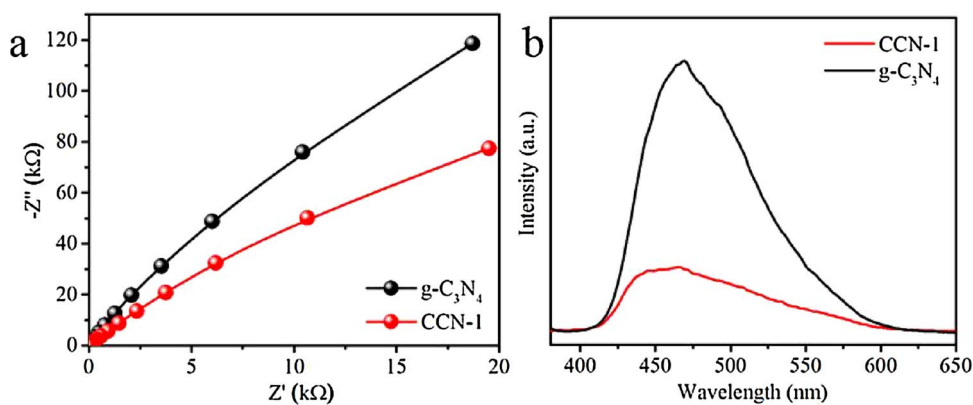
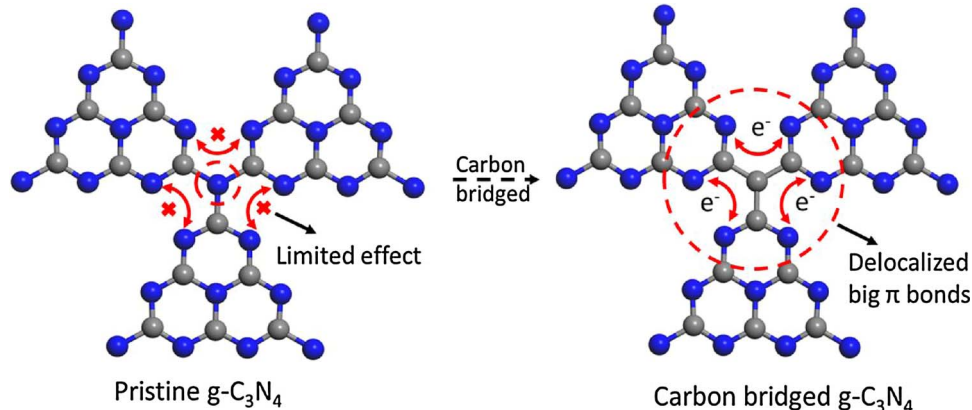


Fig. 6. (a) Photocatalytic H_2 evolution rate of pristine $\text{g-C}_3\text{N}_4$ and CCN-1; (b) comparison of HER rate of pristine $\text{g-C}_3\text{N}_4$ and CCN-x; (c) cycling HER of CCN-1 under visible light irradiation ($\lambda > 420 \text{ nm}$).

Fig. 7. (a) EIS plots and (b) PL spectra of pristine $g\text{-C}_3\text{N}_4$ and CCN-1.Fig. 8. Scheme illustration of carbon bridged $g\text{-C}_3\text{N}_4$ (C, N are indicated by grey and blue spheres, respectively).

adjacent heptazine units in CCN-1. Based on the discussion above, the excellent photocatalytic H_2 evolution activity of as-prepared CCN-x samples could be ascribed to both the enhanced light absorption and the improved charge separation by the substitution of the bridged N atoms with C atoms.

A plausible mechanism was proposed based on the above analysis, as illustrated in the schematic diagram in Fig. 8. For pristine $g\text{-C}_3\text{N}_4$, the heptazine ring units were connected by bridged N atoms, which have little effects on the electronic structures of the conduction bands or valence bands. Thus, the charge transfer between adjacent heptazine rings would be prevented. Once the bridged N atoms were substituted by C atoms (e.g., CCN-1), delocalized big π bonds would be formed owing to the contribution to the electronic structures by the bridged C atoms, which would not only act as a “physical bridge” to connect heptazine rings, but also act as an “electron bridge” to facilitate the charge transfer between adjacent heptazine rings. As a result, the π states increased and the orbital overlap become stronger, which would promote the charge transfer and separation, thereby greatly enhancing the photocatalytic activity.

4. Conclusions

In summary, we prepared carbon bridged $g\text{-C}_3\text{N}_4$ by a simple supramolecular self-assembly process. Carbon has been identified to be doped into $g\text{-C}_3\text{N}_4$ lattice by substituting the bridged N atoms based on experimental and theoretical analysis. Owing to the formation of the delocalized big π bonds, the light absorption and the charge separation in as-prepared CCN-x samples were greatly improved. As a result, the photocatalytic activity of CCN-x were greatly improved comparing to pristine $g\text{-C}_3\text{N}_4$. And CCN-1 exhibits the highest photocatalytic H_2 evolution rate of $52.9 \mu\text{mol h}^{-1}$, which is about 7 times that of pristine

$g\text{-C}_3\text{N}_4$. This work demonstrates that C self-doping can be realized through a simple supramolecular self-assembly process, by forming delocalized big π bonds, the photocatalytic activity of $g\text{-C}_3\text{N}_4$ can be greatly improved. This provides a new method for the fabrication of high efficient $g\text{-C}_3\text{N}_4$ photocatalysts for practical applications with low cost.

Acknowledgements

This work is financially supported by the National Natural Science Foundation of China (21333006, 11374190, 21573135, and 51602179), the National Basic Research Program of China (the 973 program, 2013CB632401). B.B.H. acknowledges the support from the Taishan Scholars Program of Shandong Province, and Z.Y.W. acknowledges support from Young Scholars Program of Shandong University (2015WLJH35).

Appendix A. Supplementary data

Supplementary material related to this article can be found, in the online version, at doi:<https://doi.org/10.1016/j.apcatb.2018.02.026>.

References

- [1] B. Zhang, Z. Wang, B. Huang, X. Zhang, X. Qin, H. Li, Y. Dai, Y. Li, *Chem. Mater.* 28 (2016) 6613–6620.
- [2] H. Cheng, M. Wen, X. Ma, Y. Kuwahara, K. Mori, Y. Dai, B. Huang, H. Yamashita, *J. Am. Chem. Soc.* 138 (2016) 9316–9324.
- [3] W.J. Ong, L.L. Tan, Y.H. Ng, S.T. Yong, S.P. Chai, *Chem. Rev.* 116 (2016) 7159–7329.
- [4] P. Wang, B. Huang, X. Qin, X. Zhang, Y. Dai, J. Wei, M.H. Whangbo, *Angew. Chem. Int. Ed.* 47 (2008) 7931–7933.
- [5] Z. Zheng, B. Huang, X. Qin, X. Zhang, Y. Dai, M.-H. Whangbo, *J. Mater. Chem.* 21

(2011) 9079.

[6] Z. Zheng, B. Huang, J. Lu, Z. Wang, X. Qin, X. Zhang, Y. Dai, M.H. Whangbo, *Chem. Commun.* 48 (2012) 5733–5735.

[7] H. Cheng, B. Huang, Y. Dai, X. Qin, X. Zhang, *Langmuir* 26 (2010) 6618–6624.

[8] X. Wang, K. Maeda, A. Thomas, K. Takanabe, G. Xin, J.M. Carlsson, K. Domen, M. Antonietti, *Nat. Mater.* 8 (2009) 76–80.

[9] X. Li, Y. Dai, Y. Ma, S. Han, B. Huang, *Phys. Chem. Chem. Phys.* 16 (2014) 4230–4235.

[10] Y.P. Zhu, T.Z. Ren, Z.Y. Yuan, *ACS Appl. Mater. Interfaces* 7 (2015) 16850–16856.

[11] J. Zhang, L. Qu, G. Shi, J. Liu, J. Chen, L. Dai, *Angew. Chem. Int. Ed.* 55 (2015) 2230–2234.

[12] T.Y. Ma, J. Ran, S. Dai, M. Jaroniec, S.Z. Qiao, *Angew. Chem. Int. Ed.* 54 (2015) 4646–4650.

[13] Z. Li, C. Kong, G. Lu, *J. Phys. Chem. C* 120 (2015) 56–63.

[14] L. Ye, D. Wang, S. Chen, *ACS Appl. Mater. Interfaces* 8 (2016) 5280–5289.

[15] F. Wang, Y. Wang, Y. Feng, Y. Zeng, Z. Xie, Q. Zhang, Y. Su, P. Chen, Y. Liu, K. Yao, W. Lv, G. Liu, *Appl. Catal. B: Environ.* 221 (2018) 510–520.

[16] Q. Xu, B. Cheng, J. Yu, G. Liu, *Carbon* 118 (2017) 241–249.

[17] Y. Lu, C. Ji, Y. Li, R. Qu, C. Sun, Y. Zhang, *Mater. Lett.* 211 (2018) 78–81.

[18] D. Zheng, C. Pang, Y. Liu, X. Wang, *Chem. Commun.* 51 (2015) 9706–9709.

[19] Z. Wang, W. Guan, Y. Sun, F. Dong, Y. Zhou, W.K. Ho, *Nanoscale* 7 (2015) 2471–2479.

[20] Y. Zheng, L. Lin, X. Ye, F. Guo, X. Wang, *Angew. Chem. Int. Ed.* 53 (2014) 11926–11930.

[21] S. Guo, Z. Deng, M. Li, B. Jiang, C. Tian, Q. Pan, H. Fu, *Angew. Chem. Int. Ed.* 55 (2015) 1830–1834.

[22] G. Dong, K. Zhao, L. Zhang, *Chem. Commun.* 48 (2012) 6178–6180.

[23] Z. Zhao, Y. Sun, F. Dong, Y. Zhang, H. Zhao, *RSC Adv.* 5 (2015) 39549–39556.

[24] N. Bao, X. Hu, Q. Zhang, X. Miao, X. Jie, S. Zhou, *Appl. Surf. Sci.* 403 (2017) 682–690.

[25] P. Xiao, D. Jiang, T. Liu, D. Li, M. Chen, *Mater. Lett.* 212 (2018) 111–113.

[26] Z.-F. Huang, J. Song, L. Pan, Z. Wang, X. Zhang, J.-J. Zou, W. Mi, X. Zhang, L. Wang, *Nano Energy* 12 (2015) 646–656.

[27] Y.S. Jun, J. Park, S.U. Lee, A. Thomas, W.H. Hong, G.D. Stucky, *Angew. Chem. Int. Ed.* 52 (2013) 11083–11087.

[28] C. Zhou, C. Lai, D. Huang, G. Zeng, C. Zhang, M. Cheng, L. Hu, J. Wan, W. Xiong, M. Wen, X. Wen, L. Qin, *Appl. Catal. B: Environ.* 220 (2018) 202–210.

[29] C. Yan, R. Liu, Y. Cao, C. Zhang, D. Zhang, *Ceram. Int.* 39 (2013) 3409–3412.

[30] B. Wang, C. Tian, L. Wang, R. Wang, H. Fu, 025606, *Nanotechnology* 21 (2010).

[31] G. Kresse, J. Furthmüller, *Phys. Rev. B* 54 (1996) 11169.

[32] J.P. Perdew, K. Burke, Y. Wang, *Phys. Rev. B* 54 (1996) 16533.

[33] H.J. Monkhorst, J.D. Pack, *Phys. Rev. B* 13 (1976) 5188–5192.

[34] N.E. Mircescu, M. Oltean, V. Chiș, N. Leopold, *Vib. Spectrosc.* 62 (2012) 165–171.

[35] M. Shalom, S. Inal, C. Fettkenhauer, D. Neher, M. Antonietti, *J. Am. Chem. Soc.* 135 (2013) 7118–7121.

[36] Y. Chen, B. Wang, S. Lin, Y. Zhang, X. Wang, *J. Phys. Chem. C* 118 (2014) 29981–29989.

[37] W. Gordy, *J. Chem. Phys.* 15 (1947) 305–310.

[38] W. Xing, C. Li, G. Chen, Z. Han, Y. Zhou, Y. Hu, Q. Meng, *Appl. Catal. B: Environ.* 203 (2017) 65–71.